PROCEEDINGS, 41st Workshop on Geothermal Reservoir Engineering
Stanford University, Stanford, California, February 22-24, 2016
SGP-TR-209

Fault-Controlled Damage and Permeability at the Brady Geothermal System, Nevada, USA

Roselyne C. Laboso and Nicholas C. Davatzes

1901 N. 13th Street, Beury Hall 326, Philadelphia, PA, 19122

rclaboso@gmail.com, davatzes@temple.edu

Keywords: fractures, stress, slip, Brady Geothermal Field

ABSTRACT

Identifying and locating permeable zones in geothermal fields is a critical step in determining reservoir potential for energy production. Despite a general association with active faults, geothermal systems typically display heterogeneously distributed fracture density, connectivity, and attitude – all of which influence permeability. We postulate that permeability in a geothermal system is favored in volumes of enhanced coulomb stress and reduced compression that promote high fracture density. Such volumes develop along a large active fault where slip locally perturbs the remote stress. Conversely, permeability can be inhibited in locations where coulomb stress is reduced, or where the faults are poorly oriented in the stress field and consequently slip infrequently. This paper explores the relationship between fault geometry and associated stress perturbations that result from fault slip driven by a remote stress. Our approach to predicting permeability from these local variations in stress is applied to the Brady normal fault system of Nevada, where the permeable volume is well-documented by the distribution of successful and marginal geothermal production wells, surface hydrothermal features, microseismicity, and surface deformations associated with the reservoir. The analysis is conducted using Poly3D, a boundary element program based on the three-dimensional fault geometries constructed by Jolie (2014) in a homogeneous linear elastic, half-space. The faults are loaded with remote stresses measured as part of the Brady EGS experiment and are also generally consistent with the tectonic setting and the geologic stress tensor inverted from the fault geometry and slip indicators by Jolie (2014). The simulations demonstrate a complex pattern of stress perturbation, influenced by the detailed fault geometry. Preliminary results show a correlation between regions of enhanced coulomb stress, reduction of least compressive principal stress, and successful wells, whereas low permeability wells lie outside these volumes. We further explore the promotion and suppression of fracturing observed in the models of the detailed fault geometry using idealized faults to quantify the role of segmentation, large-scale roughness, relative attitude, and stress state.

1. INTRODUCTION

Geothermal systems suitable for development as an energy source requires a heat source, saturated pore volume, and permeable zones for both transport and extraction of hot fluids from depth (Curewitz and Karson, 1997; Hanano, 2004). Typical heat sources include young volcanic bodies or metamorphic rocks within the Earth whereby faults and associated fractures can host connected porosity and support movement of fluids from heat reservoirs at depth. Through advection, hot fluids are transported along these conduits into shallower porous volume constituting a geothermal reservoir.

The Basin and Range Province of western U.S.A. is a good example of a region experiencing regional extension associated with crustal thinning that brings hot rock to relatively shallow depth. The area consists of multiple series of normal faults that dissect the shallow crust and extend to these hot rocks at depth. These vertically extensive features provide permeable connection to hot rock and contributes to pore volume needed to host a geothermal reservoir. Slip on these features can also be accompanied by dilatation and production of a network of connected pores in the form of broken rock that could enhance permeability (Caine et al., 1996). Moreover, slip on these structures can elastically distort the adjacent volume of rock, providing extensive zones of damage especially near fault tips and intersections between segments and to a lesser extent bends in faults. These more extensive volumes provide a basis for flow and storage of geothermal fluids sufficient to support a reservoir (e.g. Tamagawa and Pollard, 2008).

In the Basin and Range, as elsewhere, faults are strongly correlated with hot springs and commercially viable hydrothermal systems. However, development of these systems is impeded by highly heterogeneous permeability and temperature variations along faults. The role of large faults in supporting and focusing the circulation of geothermal fluids can be assessed to first order by examining the spatial association of faults and hydrothermal features (e.g., Curewitz and Karson, 1997; Caskey and Wesnousky, 2000; Siler and Faulds, 2013; Faulds and Hinz, 2015; Siler et al., 2015). Such features include: (1) distribution of active surface hydrothermal features include hot grounds, fumaroles, hot springs, mineralization such as sulfur, quartz, chert, and calcite, soil gases including carbon dioxide, hydrogen sulfide, radon isotopes, whereas ancient features include sinter deposits (Coolbaugh et al., 2004), (2) successful geothermal production wells that encounter high temperatures and permeable volume, (3) land surface experiencing subsidence resulting from drawdown of the water table and corresponding reduction in fluid pressure and compaction of fault rock (Ali et al., 2014; Ali et al., 2015), and (4) distribution of micro earthquakes following injection events caused by slip of fractures and faults with newly introduced fluids in the subsurface (e.g. Gaucher et al., 2015). Conversely, volumes of low permeability or volumes which lack effective connection to a heat source can be inferred from the absence of hydrothermal features or most importantly, from cold or unproductive geothermal wells.

The correlation between geometric complexities of faults and geothermal systems is well established (e.g., Curewitz and Karson, 1997). Faulds et al. (2010) investigated the structural controls on fluid flow in Brady, Desert Peak, and Desert Queen geothermal fields within the northern Hot Springs Mountains. They found that most productive wells were located in relays between fault segments and areas with multiple splays and terminations. They postulate that these volumes are characterized by high fracture density that extends

vertically along these structures providing a critical high permeability that facilitates the rise of hot geothermal fluids. Jolie (2014) extended this analysis in collaboration with Faulds and Moeck (Jolie et al., 2012) to develop a 3D geologic model of Brady. The analysis tests the association of the propensity for slip and dilation inferred from the fault geometry and the stress state with diffuse degassing processes and natural gamma radiation as an indication of local permeability. The comparison identified increased degassing rates within a left step between two fault segments that extend to the base of the model volume and below the hydrothermal reservoir tapped by production wells. Micklethwaite et al. (2010) demonstrate similar geometric associations between faults and ore deposits. The accumulation of ores suggest that the flow of hot fluid is supported for significant geologic time despite mineral precipitation through the rejuvenation of fracture porosity driven by stress localized between mechanically interacting fault segments. Their work builds on prior work by King et al., (1994), which suggests that these complex volumes of enhanced stress correlate with extensive regions of small magnitude aftershocks following the main shock on a larger fault.

In this paper, we investigate the role of large mapped faults in focusing fluid flow at the Brady geothermal system. We postulate that permeability will be developed and maintained in volumes where stress localized by fault slip promotes high fracture densities and fracture slip that can support the long-term percolation of geothermal fluids. These regions should be associated with areas of high ratio of shear to normal traction resolved on the faults by the remote stress tensor (following similar analysis by Jolie, 2014). These regions should also correlate with successful wells and other indicators of an actively flowing hydrothermal system. Conversely, areas outside these regions should have relatively little fracture development and rejuvenation. We use the boundary element method, implemented in Poly3D, to calculate local elastic stresses resulting from fault slip. We explore the sensitivity of this deformation to fault geometry. Then we apply the analysis to the detailed geometry of the Brady fault system.

2. GEOLOGIC SYNTHESIS

The analysis is conducted at the Brady Geothermal field, NV to take advantage of abundant constraints available for the modeling. The model is informed by: (1) rock mechanical properties of representative rocks (Lutz et al., 2012; TerraTek, 2011a,b); (2) measurements of the stress state from well 15-12 and 15-12ST1 during an EGS experiment; (3) fault geometry as developed by Egbert Jolie (2014), Inga Moeck, and Jim Faulds. In addition, we take advantage of multiple indicators of the relative spatial distribution of permeability mapped by previous workers. Enhanced permeability is evidenced by productive wells (Shevenell et al. 2012; Davatzes et al., 2013; Spielman pers. comm., 2015), water table draw-down, subsidence measured with InSAR (Ali et al, 2014; 2016), active or relic hydrothermal features (Coolbaugh et al., 2004; Kratt et al. 2006), diffusive outgassing of species reasonably associated with geothermal fluids (Jolie, 2014). The distribution of earthquakes monitored by the local seismometer network can also be used as a proxy for fractured, permeable volumes (e.g., Davatzes et al., 2013). Reduced permeability or the lack of connection to the hydrothermal system is evidenced by unproductive or cold wells, undisturbed water table and the lack of subsidence, and the lack of hydrothermal features.

Brady Geothermal Field is located in the Basin and Range Province of western Nevada, primarily in the northern Hot Springs Mountains (Faulds et al., 2010). Other major geothermal systems in the region are Desert Peak and Desert Queen geothermal fields that are spaced about 5 km apart. These faults offset a more then 2 km thick package of late Oligocene to late Miocene meta-volcanic and sedimentary which overlie Oligocene ash flow tuffs and Jurassic plutonic-metamorphic basement (Faulds et al., 2010; Lutz et al., 2011). The basement rocks are only exposed in the Desert Queen area where they intruded into a sequence of Triassic metamorphic rock. The hydrothermal reservoir is located in a prominent fault bend, where most production wells are clustered (Figure 1). The production wells range in depth from ~600 to 1500 m that targets Oligocene volcanics of the Chloropagus Formation and sometimes deeper rhyolite units, while injection wells are ~300 m deep and target andesitic rocks that overlies the Desert Peak Formation (Lutz et al., 2011). Recent Holocene fault ruptures on some fault segments offset Lake Lahontan sediments (Bell, 1984; Faulds and Garside, 2003) as well as associated subaqueous hydrothermal deposits (Coolbaugh et al., 2004).

While both Desert Peak and Desert Queen are blind geothermal systems, Brady has surface manifestations of hydrothermal activity (Faulds and Garside, 2003; Coolbaugh et al., 2004; Faulds et al., 2010). Active surface hydrothermal features are distributed along a complex system NE-SW to N-S trending ~4 km long fault traces. These features include fumaroles, mud pots, warm grounds, and hot springs, as well as fossil features include sinter deposits, silicified roots and algal matter, silicified bedrock, and silcrete (Figure 1). A prominent left step between these fault segments, several intersections of fault segments are associated with more aerially extensive and intense hydrothermal activity. Shevenell et al. (2012), consistent with results from Coolbaugh et al. (2004) and Jolie (2014), distinguishes two regions of hydrothermal flow: (1) deep upwelling coinciding with production wells in the left-stepping bend of the young Holocene fault scarp and a region of subsidence revealed by InSAR (Davatzes et al., 2013; Ali et al., 2016); (2) shallow outflow associated with distributed hot ground and active fumaroles along this fault trace and was enhanced by drilling activities in the 1970's. However, only a small number of the numerous faults breaking the surface, and their intersections and bends, are associated with these features.

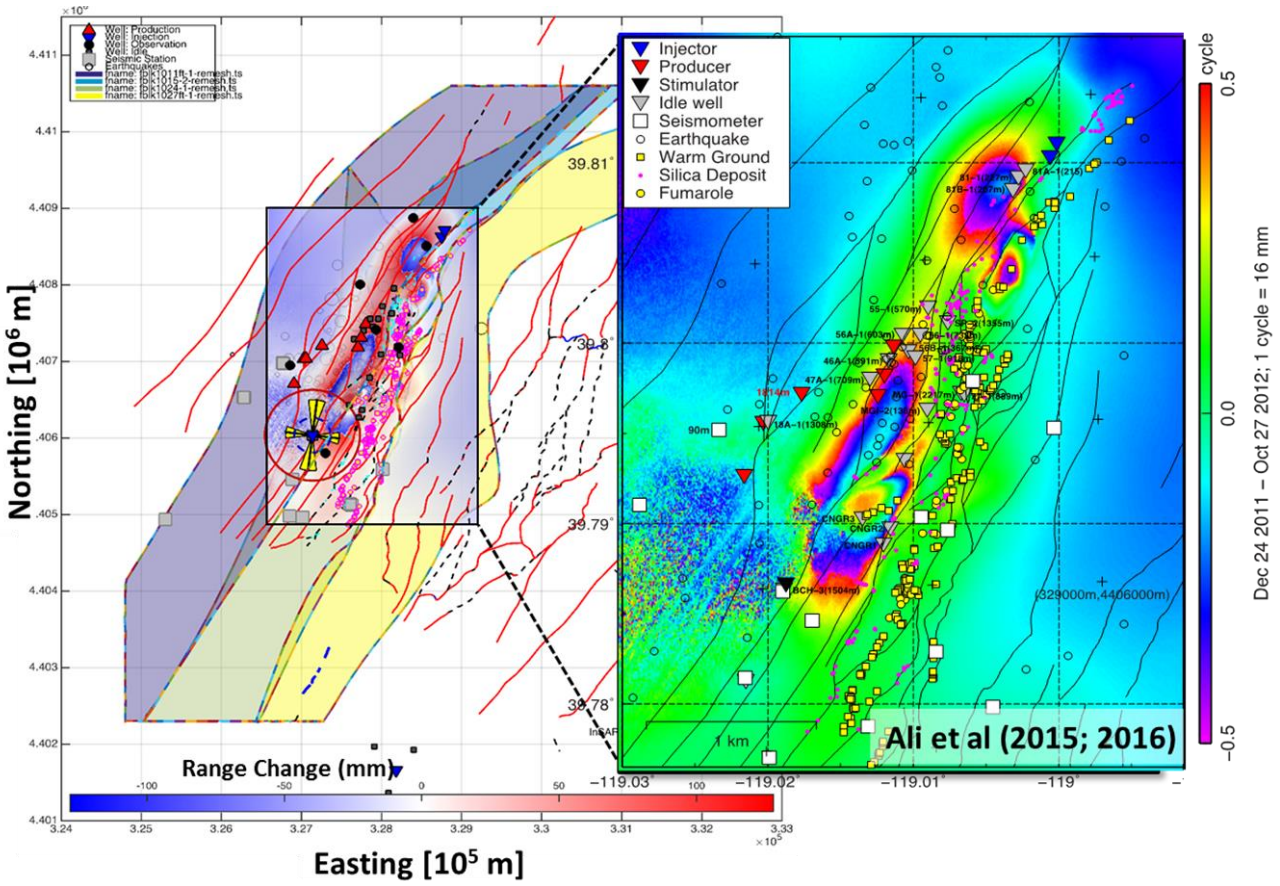

Figure 1: Map of Brady Geothermal Field with faults from Faulds et al. (2010), selected 3D fault geometries from Jolie (2014), surface hydrothermal activity from Coolbaugh et al. (2004), subsidence imaged by InSAR modified from Ali et al. (2015, 2016), and wells from ORMAT (personal communication E. Zemach, 2011), and summary of the stress state normalized to the lithostatic load from Moos (2010, unpublished stress model for the Brady EGS project). Purple and blue faults dip west, whereas yellow fault dips to the east. Red triangles are active production wells, blue triangles are active injection wells, grey triangles are idle wells, purple and yellow squares are surface hydrothermal features. Purple dots and yellow squares are hydrothermal features. Gray/white squares are seismometers. The inset interferogram in red-white-blue represents surface deformation in the line of site of the satellite resulting from geothermal production between 1997 and 2002, where one color fringe corresponds to one TerraSAR x-band cycle of phase change corresponds to 16 mm of range change (Ali et al., 2014).

Seismicity is observed and monitored by seismometer arrays managed by Lawrence Berkeley National Laboratory (Nathwani et al., 2011; Davatzes et al., 2013; http://esd1.lbl.gov/research/projects/induced_seismicity/egs/bradys_hot_springs.html). Micro-earthquakes (MEQ) in the geothermal field tend to occur episodically, distributed along the trend of the fault associated with surface hydrothermal features and Holocene fault scarps, roughly from the injection wells in the NNE to the production wells in the SSW (Davatzes et al., 2013; Ali et al., 2015; Davatzes et al., 2015) (Figure 1). Tracer analysis suggests that this is the path of fluid transport between injection and production wells (GeothermEx 1992; Davatzes et al., 2013). The largest MEQs occur nearer the injectors or deep below the production area, whereas the majority of events occur in the production area along a vertically extensive volume more than 2 km tall (Figure 2). The events in the production area occur between the dominant fault segment and an abutting fault segment which both dip to the west.

Brady Geothermal Field has been in continuous operation since 1992 and supports a combined dual flash and binary geothermal power plant with a total installed capacity of 26 MWe (Faulds et al., 2010). Presently, there are six operational production and two injection wells tapping water from depths of ~0.5-1.2 km depth over a horizontal distance of approximately 0.5 km. An EGS well 15-12ST-1, located SW of the production wells was stimulated in an attempt to increase power generation at Brady. Downhole temperature is measured 204°C (400°F) at ~ 1.3 km depth in 15-12ST1 and 177°C (350°F) at 0.15 to 1.2 km in the production volume. Well 15-12ST1 was drilled in 2007. From that time until stimulation in 2013-2014, the relative water table, temperature and tracer testing indicate that 15-12ST-1 is isolated from the production volume (Davatzes Pers. Comm., 2015; Geothermex, 1992).

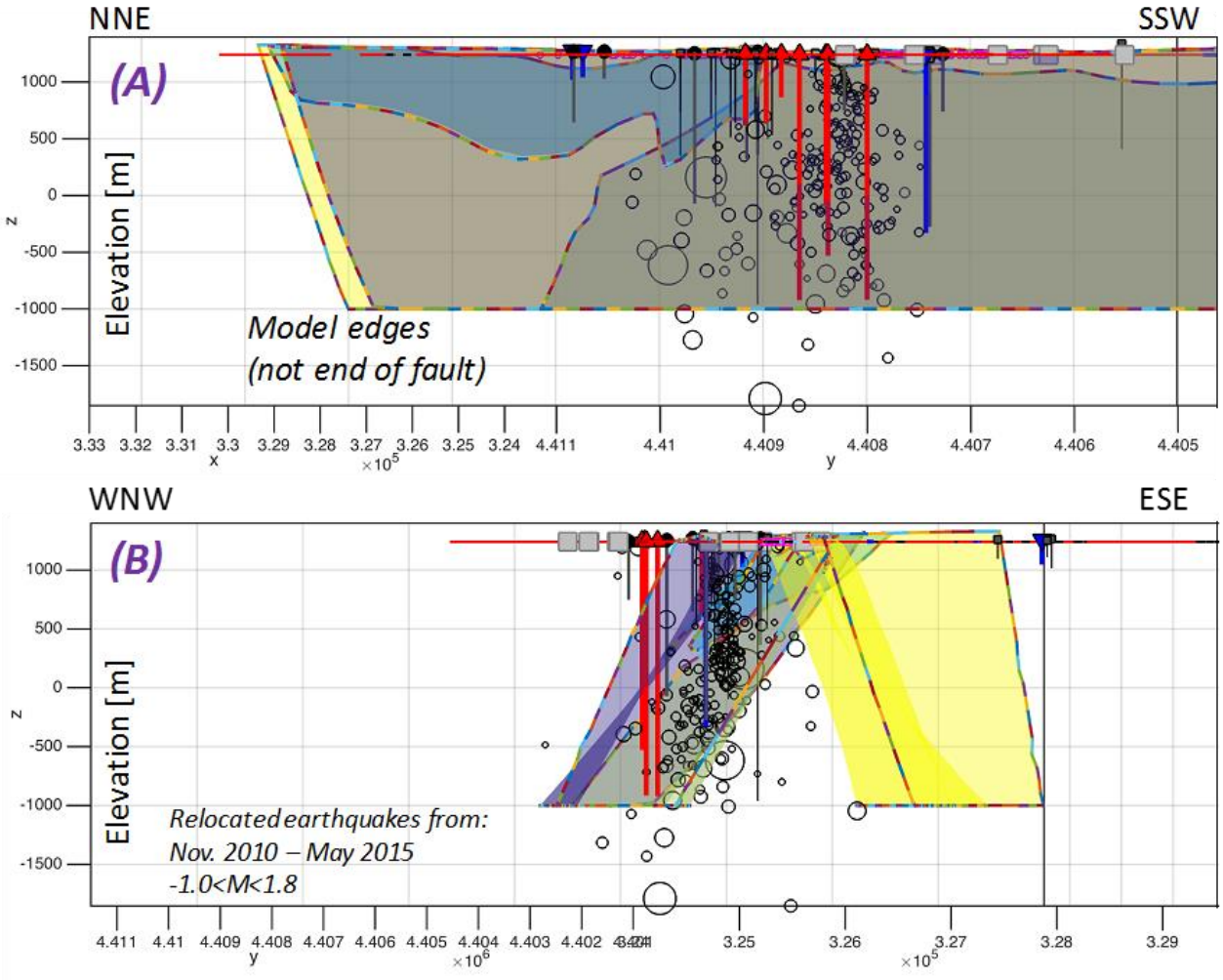

Figure 2: Cross-section views of selected faults from the 3D geologic model of Jolie (2014) the three dimension fault model oriented normal (a) and parallel (b) to the predominant fault strike (Figure 1). From the 61 faults in the model, 4 planes have been selected for the strong association with seismicity, recent fault slip, earthquakes, subsidence, and hydrothermal surface features. Model is constructed in NAD83 and UTM Zone 11N.

3. METHODS

3.1 BEM Modeling of Fault Slip and Stress

The displacement discontinuity boundary element method (BEM) as described by Crouch and Starfield (1983), and implemented in Poly3D (Thomas, 1993) is used to model fault slip and related elastic deformations. Poly3D solves the numerical boundary value problem relating quasi-static far field stress or strain, displacement discontinuities or tractions on boundary elements, and the resulting deformation or stress field in a continuous, linear elastic, isotropic and homogeneous half-space. In this application, triangular boundary elements are used to define discrete faults capturing their complex geometry (Figure 3a). We prescribe zero shear traction and zero normal displacement (no opening or interpenetration) on each triangular element and solve for slip and normal tractions induced by a far field remote stress applied to induce deformation. Young's modulus and Poisson's Ratio define the response of the elastic continuum, which is calculated at discrete observations points to simulate the local displacement, strain, and stress fields. Element size minimized near observation points and for modeling closely spaced, strongly interacting fault segments to improve model resolution and stability by avoiding numerical artifacts associated with element edges (Figure 3b).

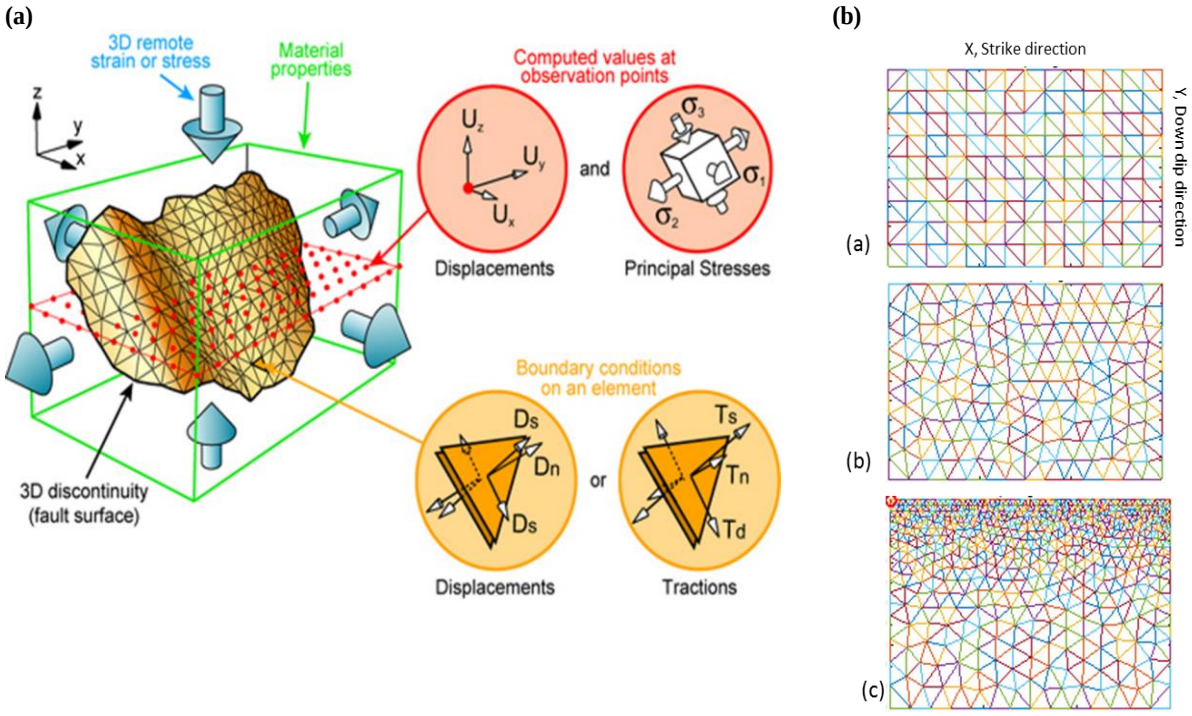

Figure 3: (a) Summary of Poly3D model configuration (courtesy of Laurent Maerten) with a curved fault plane with irregular edges in 3D space discretized into triangular elements. Boundary conditions at the fault can be specified as displacement discontinuity or tractions. Complimentary values of displacement discontinuity and tractions are calculated at element centers. Resulting displacements, strain and stress in the surrounding continuum are calculated at observations points (red dots). (b) Example wireframe meshes employed for idealized model of fault geometries.

***Table 1**: Modeled parameters for sensitivity analysis.*

Parameter	**Magnitude** (and Uncertainty)	**Units**	**Source**
Geometry of Detailed Fault Model			Jolie et al (2012); Jolie (2014)
Minimum element edge length	250	m	
Geometry of Idealized Faults			
Minimum element edge length	250	m	
Fault dip	60	degrees	
Fault strike	025	azimuth	
Fault height	5000	m	
Fault strike length	~14000	m	
Remote Stress Field Components (at 1250 m depth) *			Moos et al.(2011, unpublished report)
S_v	29.4	MPa	
S_{Hmax}	22.1	MPa	
S_{hmin}	15.3	MPa	
Pp	11.3	MPa	
S_{Hmax} azimuth	007 ± 13	azimuth	
Stress model depth	1250	m	
Elastic Properties			Lutz et al. (2010,2011); TerraTek (2011)
Young's Modulus	80	GPa	
Poisson's Ratio	0.23	unitless	
Strength			Lockner and Beeler (2002); Lutz et al. (2010,2011); TerraTek (2011)
Friction	0.83 to 0.93	unitless	Over all depths: 0.55 to 0.93
Cohesion	0 to ~7.4	MPa	Over all depths: ~7.4 to 34

** stress tensor and pore pressure values are reported in geologic compression positive convention.*

We simulate the map-view, local stress field at reservoir depths of 1250 m, at a 300 m depth relevant to surface hydrothermal activity and subsidence (Ali et al., 2016), as well as cross sections normal to the faults and along well trajectories. In this study, the results of analyses at 1250 m are presented. The stress field is derived from the analysis of Moos et al (2011, unpublished report) as part of the Brady EGS project at well 15-12ST1 (Table 1, Figure 1). Their analysis indicates a normal faulting stress regime where the vertical stress is the most compressive principal stress, S_V, and the least compressive principal stress is the minimum horizontal stress, S_{hmin}. Elastic properties and friction are primarily derived from testing of core in BCH-1 as part of the Desert Peak and Brady EGS projects. The ratio of principal stresses given by S_V and S_{hmin} in the 15-12ST1 stress model indicates a critical coefficient of friction given by (e.g., Zoback, 2007):

$$\frac{\sigma_1 - P_f}{\sigma_3 - P_f} = \frac{S_v - P_f}{S_{hmin} - P_f} \leq \left[\sqrt{(\mu^2 + 1)} + \mu\right]^2 \tag{1}$$

where P_f is the measured fluid pressure from equilibrated pressure logs and μ is the static coefficient of friction. The stress model implies that fractures with a coefficient of friction less than approximately 0.83 will slip if the water table is at the surface, which is reasonable for the recent past since hot springs flowed to the surface at Brady until the 1970s (Benoit et al., 1982) and prior to that Lake Lahontan inundated this region as evidenced by diatom deposits above the elevation of the production wells in the surrounding hills. Since our goal is to model the development and maintenance of fractures over geologic time, this is the most relevant scenario. For water levels 100 m below the surface representing drawdown due to geothermal production, this threshold drops to 0.74. This range significantly overlaps the range of friction measured by Lutz et al (2011) in core from Brady from 0.55-0.93, suggesting established, well-oriented fractures lacking cohesion should be critically stressed for shear failure.

3.2 Approach to Predicting Fractures from Simulated Local Stress

Fault complexity, including segmentation, overlap and intersections are clearly contributors to the mechanical interactions that promote damaged volumes of rock. However, it is also clear that while some regions of fault complexity host hydrothermal systems, the majority do not (Figures 1 and 2). In order to better understand this variability, we first use idealized models to systematically vary the geometry of segmentation and its relationship to the remote stress tensor. The idealized models provide a means of assessing the relative importance of different geometric characteristics evident in the fault system at Brady. From these models we derive the sensitivity of key predictors of fracturing on these geometric parameters.

Second, we model slip and resulting distortion on a select subset of faults from the geometric model of Brady developed by Jolie et al (2012) and Jolie (2014). For this investigation, we focus on a subset of faults directly associated with evidence of permeability as summarized in Section 2.

3.3 Criteria to Assess Fracture Slip or Opening

3.3.1 Slip on Optimally Oriented Fractures, Maximum Coulomb Stress

To further characterize and evaluate brittle deformation in the rock volume adjacent to faults, we assess the potential for frictional failure through the coulomb stress, S_c, and change in coulomb stress, ΔS_c, calculated from model output principal stress components (King et al., 1994; Crider and Pollard, 1998; Jaeger et al., 2007; Zoback, 2007). We adopt and then test the argument that fractures critically stressed for shear failure are preferentially permeable (Barton et al., 1995; Heffer, 2002). S_c is a measure of the relative production of fractures and fracture slip. This is a threshold criterion such that S_c above some critical limit exceeds either the frictional strength of established fractures or the strength of the intact rock mass if cohesion is included. In this analysis, we focus on the potential for recurring slip on established fractures consistent with abundant mapped faults and fractures visible in image logs of 15-12 and 15-12ST1 and core and so only consider friction. Friction is provided directly to the equation and also determines the optimal attitude of failure planes with respect to the stress tensor. The criterion also requires that the resolved normal traction is compressive so that friction applies as the limiting strength resisting permanent deformation. The magnitude of S_c and ΔS_c are determined respectively by:

$$S_c^{(max)} = \left(\frac{\sigma_1 - \sigma_3}{2}\right)\sqrt{(1 + \mu^2)} - \mu\left(\frac{\sigma_1 + \sigma_3}{2}\right) \tag{2}$$

$$S_c^{(max)} = \Delta\tau - \mu\Delta\sigma \tag{3}$$

where σ_1 is the greatest principal stress, σ_3 the least principal stress, μ is the coefficient of static friction (Byerlee, 1978), $\Delta\tau$ is change in shear traction and $\Delta\sigma$ is change in normal traction compared to the remote stress tensor. In this formulation, positive $Sc^{(max)}$ indicates shear traction exceeds resistance to slip, whereas negative $Sc^{(max)}$ indicates stability and suppression of slip on optimally oriented fractures. We also interpret high magnitudes of $Sc^{(max)}$ to indicate regions likely to have high fracture density (Maerten et al., 2002).

3.3.2 Tension and Opening-Mode Failure

σ_3 is used to identify tension that promotes opening-mode fracture and facilitates dilation supporting reservoir porosity and permeaiblity. In general, rock is weak in tension. The presence of flaws in naturally heterogeneous rock such as pores and established fractures concentrate tension so that even a relatively modest imposed tension can lead to localized failure of the rock mass. This is consistent with the general lack of tension measured in the earth from well data. For relative large volumes compared to the flaw

dimensions, the presence of such flaws is highly likely and thus we assume that even modest magnitudes of tension would lead to tensile failure. Thus the critical condition is $\sigma_3 < 0$.

3.3.3 Slip potential on Mapped Faults with complex geometry

Actively slipping faults are likely to be associated with enhanced permeability. However, the complex structure of well-developed faults, including development of a core characterized by a distinct fault rock as well as a surrounding zone of damaged host rock, complicates their hydrology (e.g., Caine et al., 1996). The relative stability of fault surfaces can be assessed for a given stress state by calculating the ratio of shear traction to effective normal traction. If this ratio exceeds the frictional strength of the rock, the fault is unstable or critically stressed (Morris et al, 1996). Slip tendency is expressed as a ratio of shear traction to effective normal traction resolved on a plane of weakness derived from its attitude relative to the stress tensor as:

$$S_{Tendency} = \frac{T_s}{(T_n - P_f)} \geq \mu \tag{4}$$

where (T_n - P_f) is the effective normal stress terms, and T_s is shear stress adopting a standard geologic sign convention.

3.3.4 Dilation potential on Mapped Faults with complex geometry

Dilation can accompany slip on rough fractures surfaces if the asperities of the fracture are sufficiently strong compared to the loads they must support. Thus, dilation tendency is suppressed by increasing normal tractions (Jaeger et al., 2007):

$$D_{Tendency} = \frac{(\sigma_1 - T_n)}{(\sigma_1 - \sigma_3)} \tag{5}$$

Thus the dilation tendency indicates the conditions least likely to break asperities during frictional slip, thus allowing for dilation to accompany slip on rough fracture surfaces. As $T_n$approachesσ_3, this ratio approaches 1. Note that this ratio does not explicitly express a sensitivity to the magnitude of σ_3 or to a measure of asperity strength, and so it is primarily a qualitative indicator that emphasis the fault or fracture attitudes most prone to dilation in a given stress state. Because we infer dilation to accompany slip, and not that stresses are entirely compressive, we currently restrict our analysis of dilation tendency to the portions of faults where slip tendency exceeds the frictional resistance to sliding.

4. RESULTS

Modeling idealized fault geometries representative of key portions of the Brady system in the observed modern stress state is conducted to test the sensitivity of $S_c^{(max)}$ and σ_3. This analysis also reveals the geometries that optimize these criteria and the related map extent over which these criteria predict active fracture. First, we evaluate various combinations of overlap, separation, and sense of step-over between fault segments. In these analyses, the model faults dip angle is 60^0, fault strike is 225, fault length and height are fixed and the stress tensor is fixed to the observed values at 1250 m depth (see Table 1). Second, we model the detailed geometry of selected segments from the Brady fault system to determine their impact on stress in the vicinity of production.

4.1 Fault Geometry and Overlap Analysis

The highest production rates come from a relatively small left-step of approximately 600 m separation normal to strike. Similarly, seismicity in the vicinity of the production wells is localized between the purple and green fault segments illustrated in Figures 1 and 2, characterized by a strike-normal separation of approximately 700-1000 m and extensive strike-parallel overlap.

Here we focus on understanding the interaction of such overlapping faults at Brady by systematically varying the overlap, separation and strike of a pair of idealized fault segments to assess their influence on $S_c^{(max)}$ and σ_3. The idealized faults consisting of simple planar rectangles of fixed height, length, and dip (e.g., as in Figure 3b) are subjected to the mechanical conditions at Brady (Table 1). The ideal fault geometries investigated include: (1) pairs of parallel faults with various along strike overlap (o) and horizontal, strike-normal separations (s) (examples in Figure 4); (2) overlap faults with opposed dip directions defining horsts or grabens; (3) overlap faults where one segment has a fixed strike and the other strike of the other segment varies (examples in Figure 5); and (4) a range of S_{Hmax} azimuth of double the standard deviation of the original azimuth is explored while the stress tensor, fault dip, and fault attitude is fixed (examples in Figure 6). For each simulation we track the magnitude of the local stress perturbations. In addition, we determine the position and map area over which the critical threshold of each parameter is exceeded (examples in Figure 5 and 6). In addition, the maps of $S_c^{(max)}$ and σ_3 provide a useful comparison to the mapped geologic evidence of permeability. Several hundred to a thousand combinations of these parameters are explored for each case to summarize the sensitivity.

4.1.1 Overlap and Separation

Overlap and separation among parallel and non-parallel fault segments directly influence the degree of mechanical interaction among faults and surrounding volume. In general, faults strongly interact when they are within 1 to 3 half lengths of each other, although the spatial pattern of stress perturbation must be considered (Figure 4, 5, and 6). In addition the overlap and separation appear to strongly define the size of the volume perturbed so that the potential reservoir of fractured rock is well mapped in these simulations.

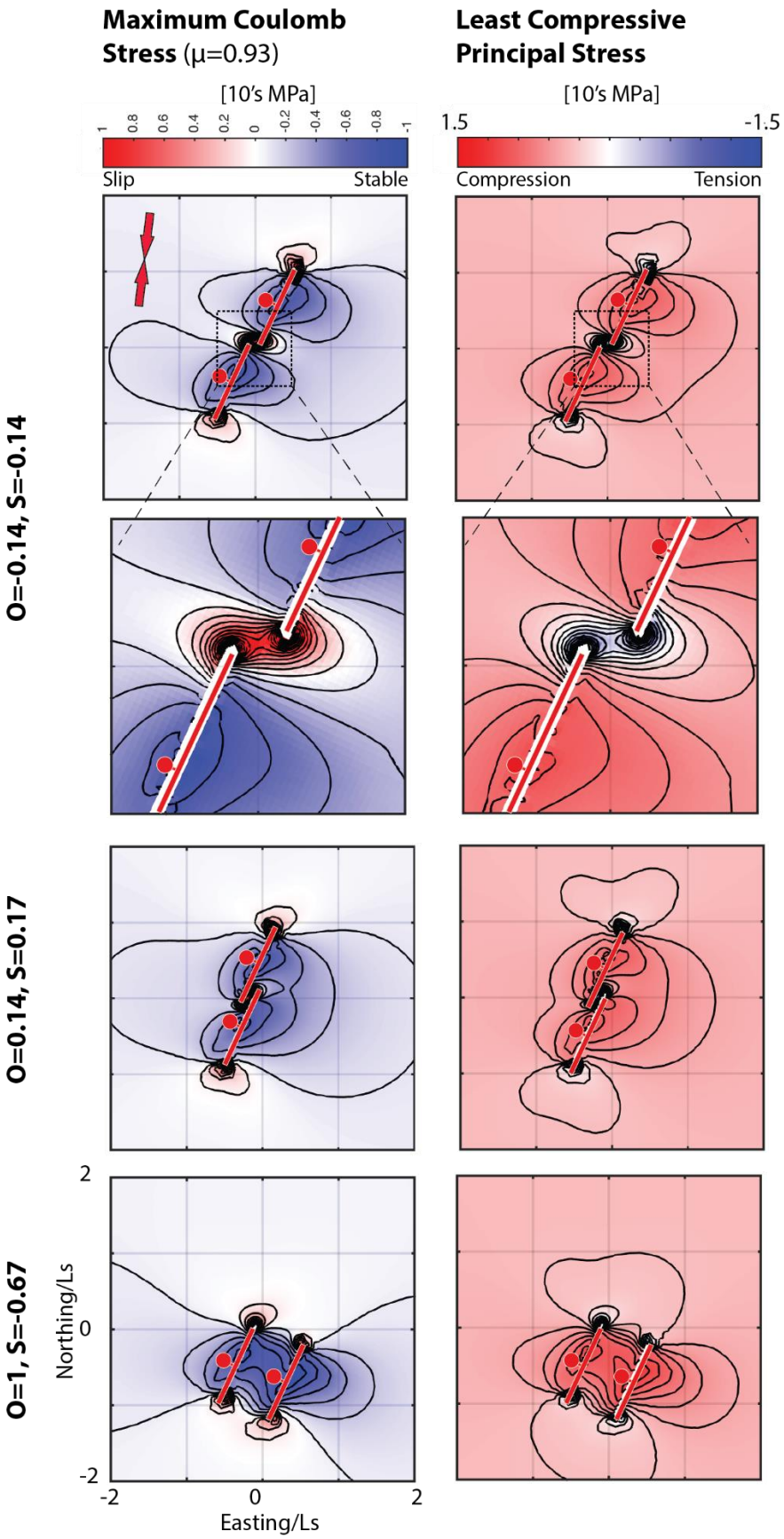

Figure 4: Example fault overlap and separation analysis for parallel faults (contour plot of $\Delta S_c^{(max)}$ and S_{hmin} at the 99th percentile).

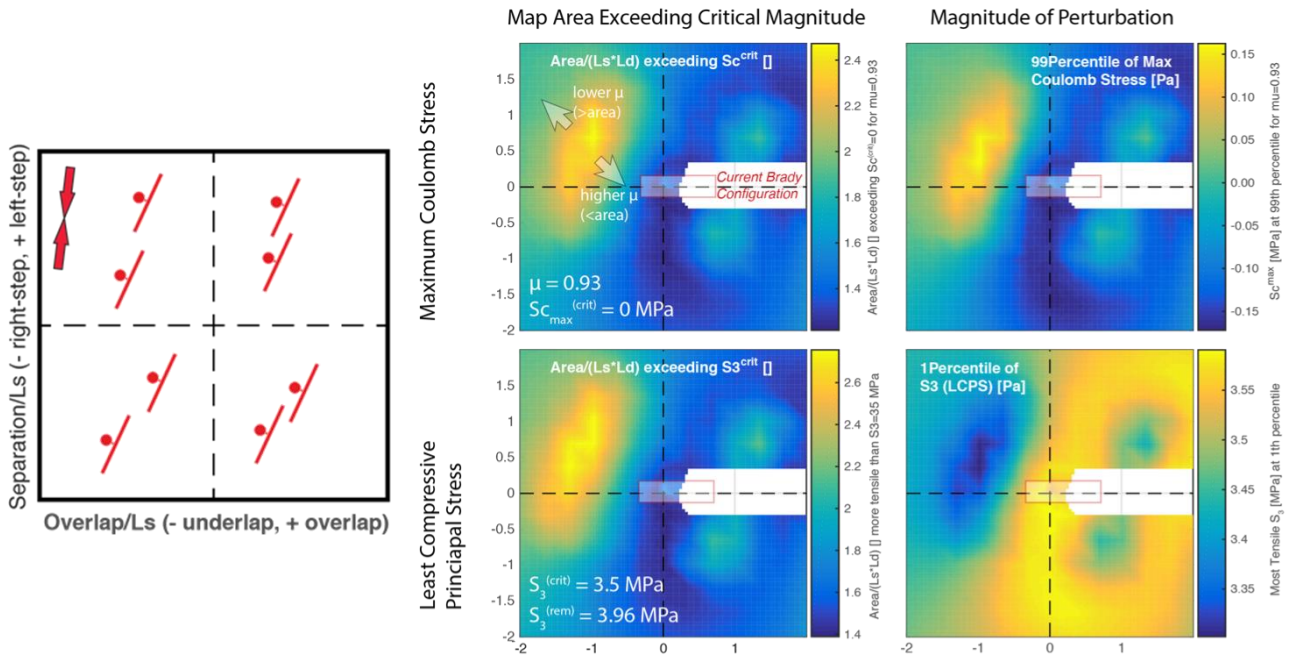

Figure 5: Summary of overlap and separation analysis of en echelon (sub-parallel) faults in both left and right steps for S_{Hmax} azimuth of 007, general fault strike of 025, and model observation depth of 1250 m. Left: Cartoon of overlap and separation organization by quadrant, and (right) summary of the results of idealized fault geometry to map area exceeding critical magnitude and magnitude of perturbation for maximum coulomb stress and least compressive principal stress at the 99th and 1st percentile respectively for a coefficient of friction of 0.93.

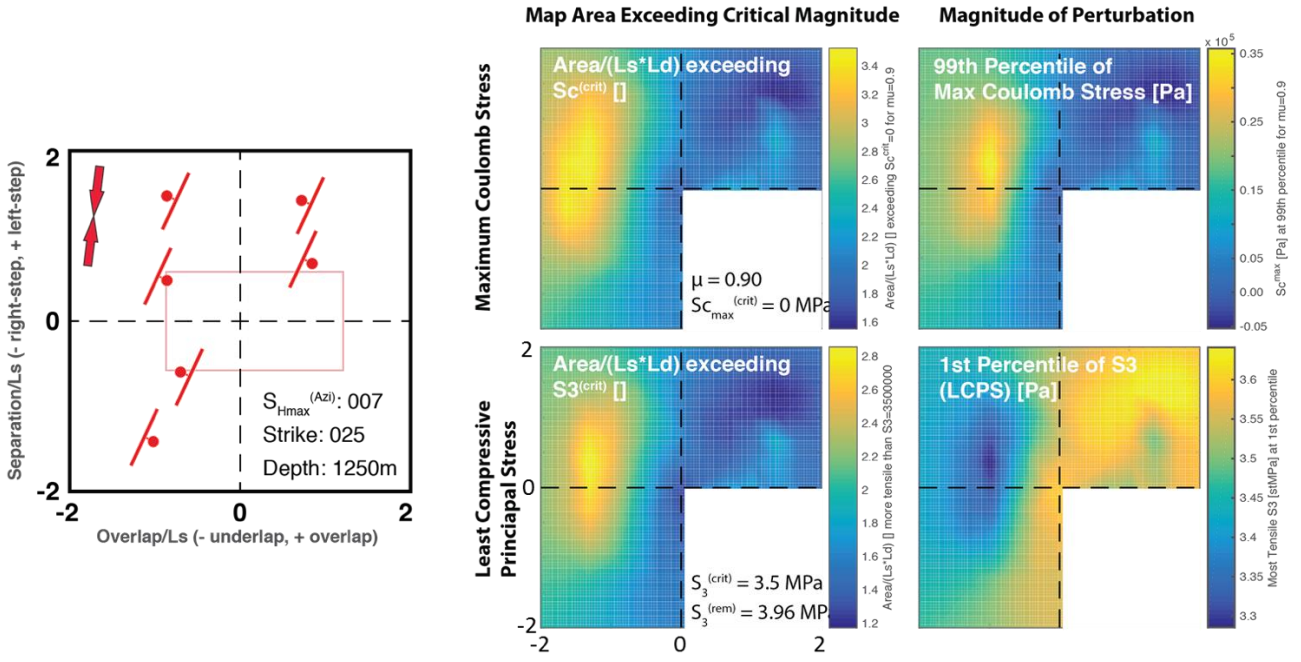

Figure 6: Summary of overlap and separation analysis on horst faults dominantly in a left step for S_{Hmax} azimuth of 007, general fault strike of 025, and model observation depth of 1250 m. (Right) Summary of the results of map area exceeding critical magnitude and magnitude of perturbation for maximum coulomb stress and least compressive principal stress at the 99th and 1st percentile respectively for a coefficient of friction of 0.90.

4.1.2 Relative Strike of Fault Segments

Many fault segments at Brady form overlapping and abutting geometries resulting from differences in strike (Faulds and Garside, 2003). We investigate these relationships by modeling fault segments where one has a fixed strike while the other varies for a given range (e.g.

~200^0 rotation) of fault orientation (Figure 7). Fixed parameters in this analysis includes stress tensor, S_{Hmax} azimuth, orientation of one of the fault segments, dip angle, and stress model depth.

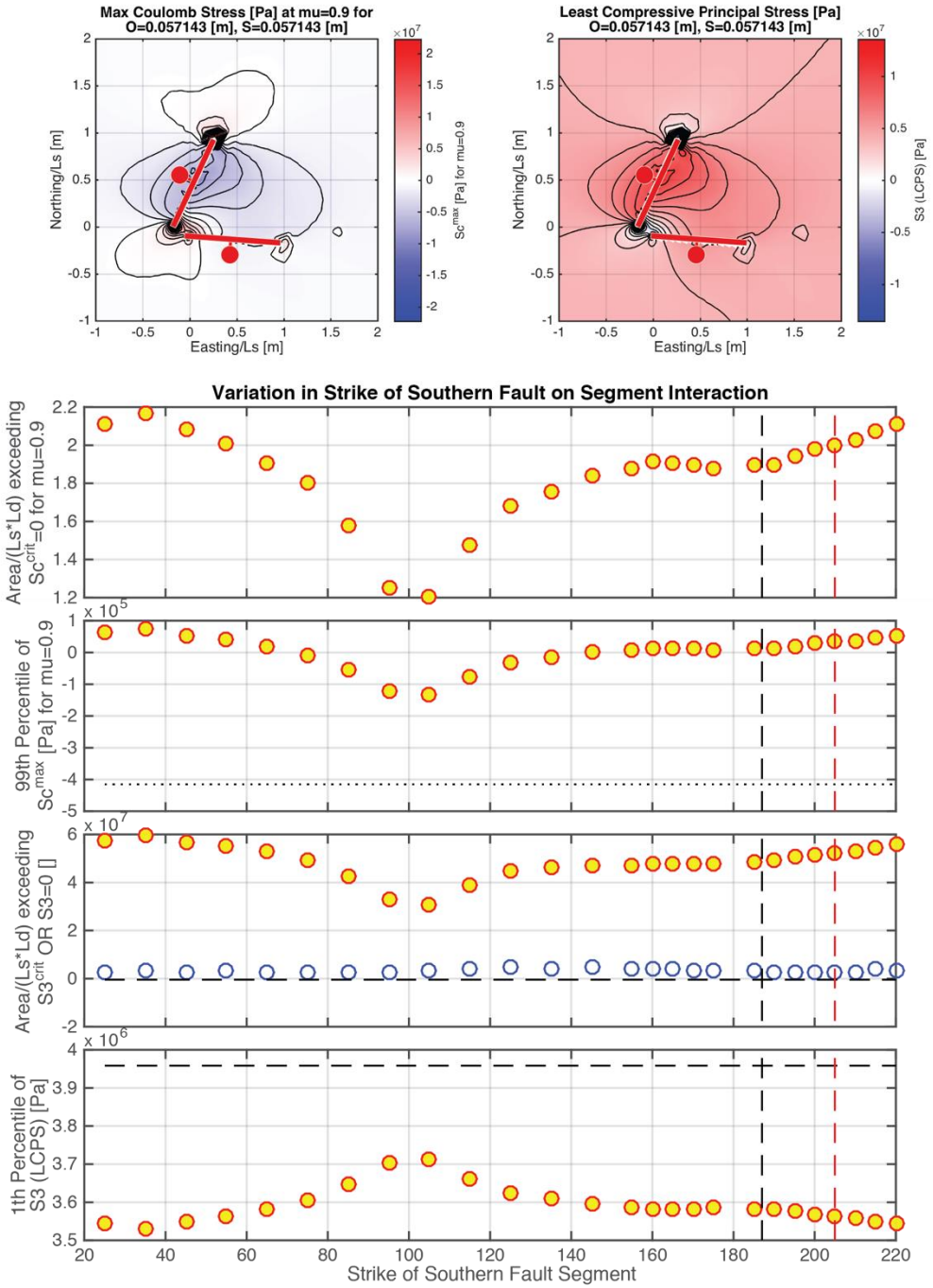

Figure 7: Example fault attitude analysis (contour plot of $S_c^{(max)}$ and S_{hmin} at the 99th percentile) and summary of variation as a function of the strike of the southern fault segment.

4.1.3 S_{Hmax} Azimuth Relative to Fault Strike

We investigate the impact of variation in S_{Hmax} azimuth on stress perturbations in the rock volume adjacent to ideal faults revealing the relative impact of strike slip and normal slip on the pattern of stressing. The reported S_{Hmax} azimuth range, 7 ± a standard deviation of 13^0 obtained from analysis of image logs in 15-12ST1 for the Brady's EGS experiment. For these simulations we model S_{Hmax} azimuth across ± two standard deviations, which includes a change in the sense of strike slip motion from left lateral to right lateral where S_{Hmax} azimuth increases beyond the strike of the model faults of 025. We maintain fixed fault dimensions and attitude and principal stress magnitudes (Figure 8 and 9).

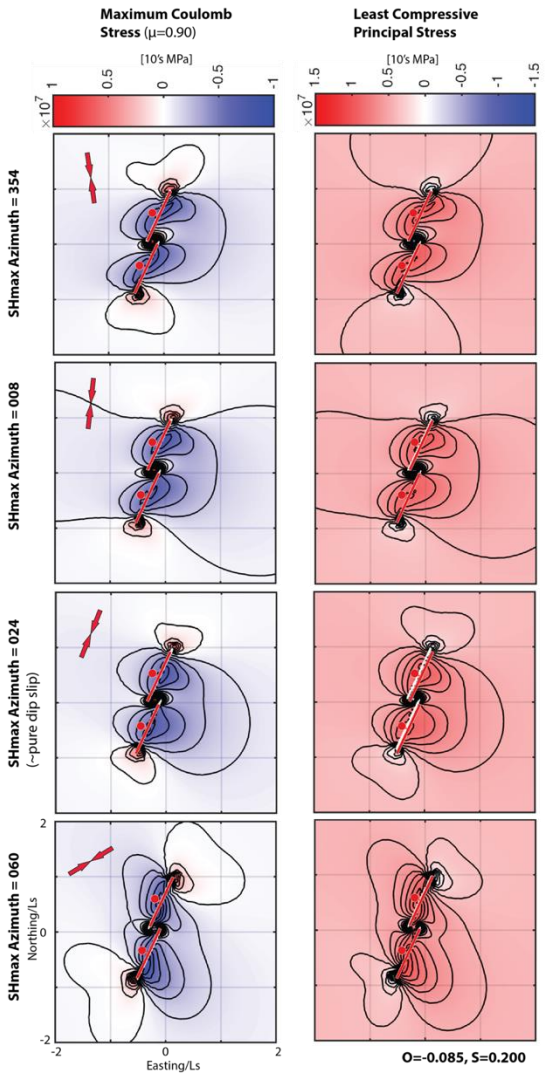

Figure 8: Example S_{Hmax} azimuth analysis (contour plots of $S_c^{(max)}$ and S_{hmin} at the 99th percentile).

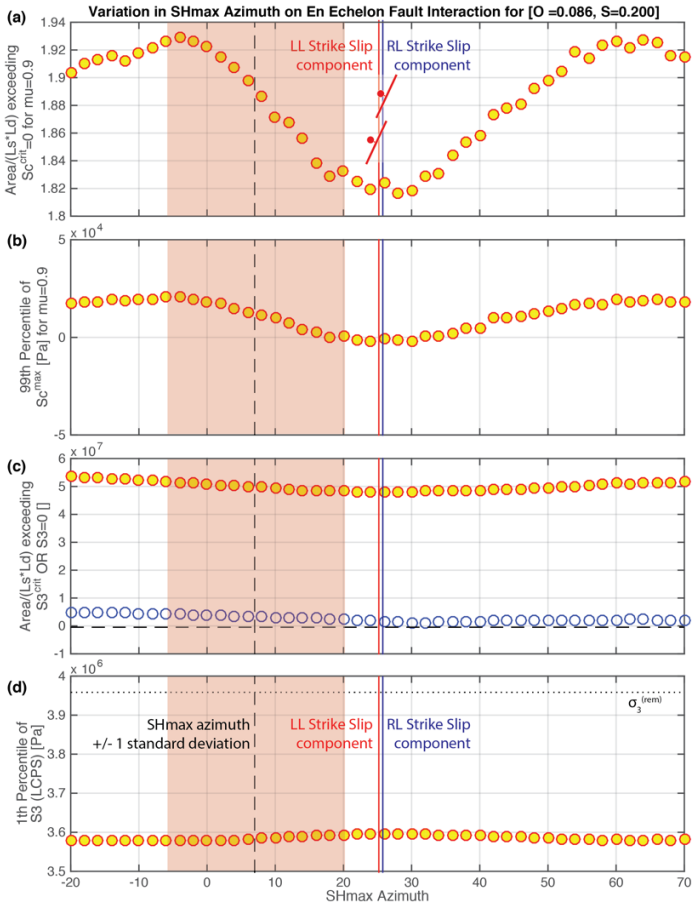

Figure 9: Summary S_{Hmax} azimuth analysis for each criterion as discussed above.

4.2 Detailed Fault Analysis

Fault segments associated with young scarps, hydrothermal manifestations, seismicity, and subsidence are modeled to determine their impact on the local stress state. For our purposes, we establish criteria to determine which of the numerous faults at Brady to model, which include: (1) The faults should have indicators of recent slip e.g. fault scarps in young sediments or offset hydrothermal deposits, (2) fault hierarchy, which ranks faults by the relative size so that large, horizontally extensive and vertical faults receive higher rank and relative age based on abutting and cross cutting relationships; (3) orientation of modern stress field that appears to promote or inhibit slip and dilatation; (4) spatial association to proxies for permeability (e.g. surface hydrothermal features and successful / failed wells) and active deformation including subsidence and MEQ activity. Four faults with these criteria (Figure 1) are modeled in their spatial location and stress perturbation patterns and analyzed.

4.2.1 Analysis of tractions resolved on the mapped faults

Faults at Brady display complex three dimensional geometry characterized by large local variations in strike and dip. This results in large localized changes in slip and dilation tendency (Figures 10 and 11). The potential range of shear and effective normal tractions are summarized on the 3D Mohr circle diagram in Figure 10. The diagram reveals a large range of potential combinations of shear and normal traction that exceed the lower frictional strength measured at Brady and relevant to the model depth of 1250 m but which are insufficient to cause frictional failure on the strongest rocks. The normal associated with each triangle discretizing the main hydrothermal fault (purple fault in Figures 1 and 2) are plotted for references. The analysis demonstrates that only portions of the fault are critically stressed. Figure 11 summarizes the variation in slip and dilation tendency across the surfaces of the most hydrothermally significant faults in Figures 1 and 2.

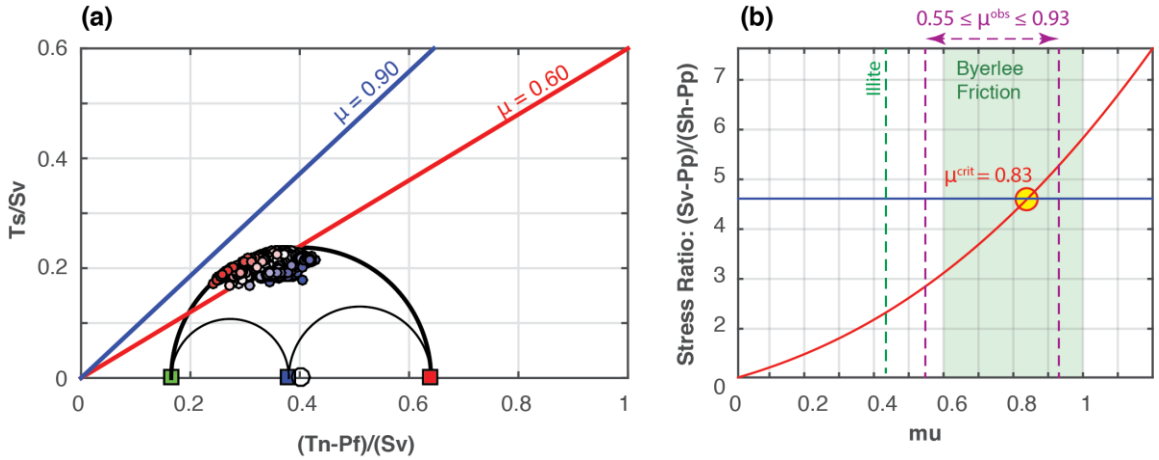

Figure 10: (a) Stress model from 15-12ST1 (see Table 1) reveals related frictional failure envelopes spanning the range of measured frictional resistance to sliding for water table to the surface. (b) Where the friction function (red line) in equation 1 exceeds the ratio of principal stresses (blue line) optimally oriented fractures are stable. Thus stress model show that optimally oriented, cohesionless fractures with μ≤0.83 will slip.

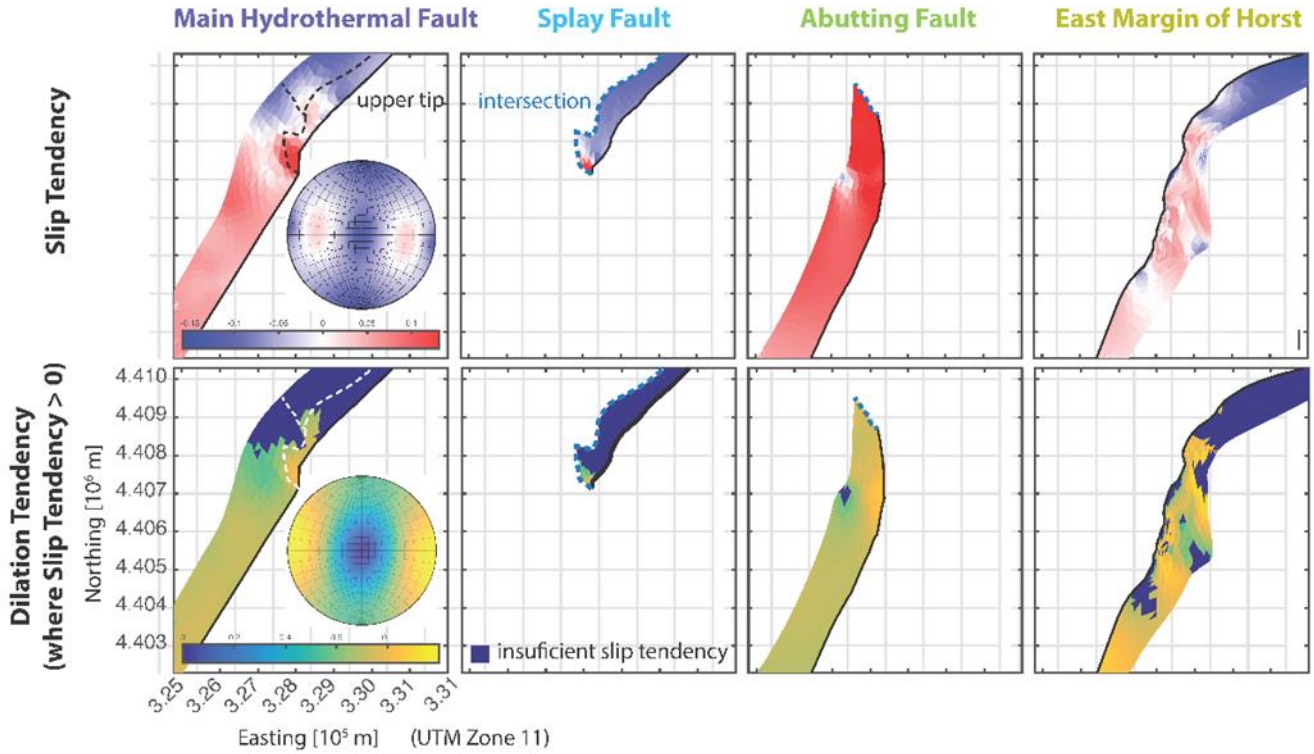

Figure 11: Summary of slip tendency (upper row) and dilation tendency (lower row) on key faults in the geothermal system. Slip tendency is assessed with respect to μ=0.6. Dilation tendency is assessed in areas subjected to a positive slip tendency. Inset stereograms are equal area, lower hemisphere projects of the direction dependence of slip tendency and dilation tendency.

4.2.2 Patterns of slip around non-planar faults

Figure 12 explores the stress that results from the main hydrothermal fault and the abutting fault, which are both spatially associated with hydrothermal features and evidence of recent slip, have high slip and dilation tendency, bracket a significant portion of MEQ hypocenters, and coincide with active subsidence and production wells (Figures 1 and 2). The main fault largely lowers $\Delta Sc^{(max)}$ in vicinity of the production wells despite the presence of the prominent bend (Figure 12a,b). It appears that bends in the interior of normal faults, even with some strike slip component that should promote dilation, due to the combination of left-stepping geometry with left-lateral strike slip component, have negligible impact here. This is consistent with analysis at an even more extreme fault bend at Desert Peak by Swyer and Davatzes (2012, 2013) under similar geomechanical conditions. Similarly, the examples from the segmented idealized faults suggest that un-breached relays and fault tips provide key regions of enhanced stress. In this location, the abutting

segment does roughly enhance $\Delta Sc^{(max)}$ near active production (Figure 12c,d). It remains to be seen how fully interacting slip among the pair of faults perturbs the local stress state. Although the overall relationship is clear, complex mechanical interaction clearly makes it difficult to intuit which locations are likely to be highly fractured and permeable without a complete geomechanical analysis.

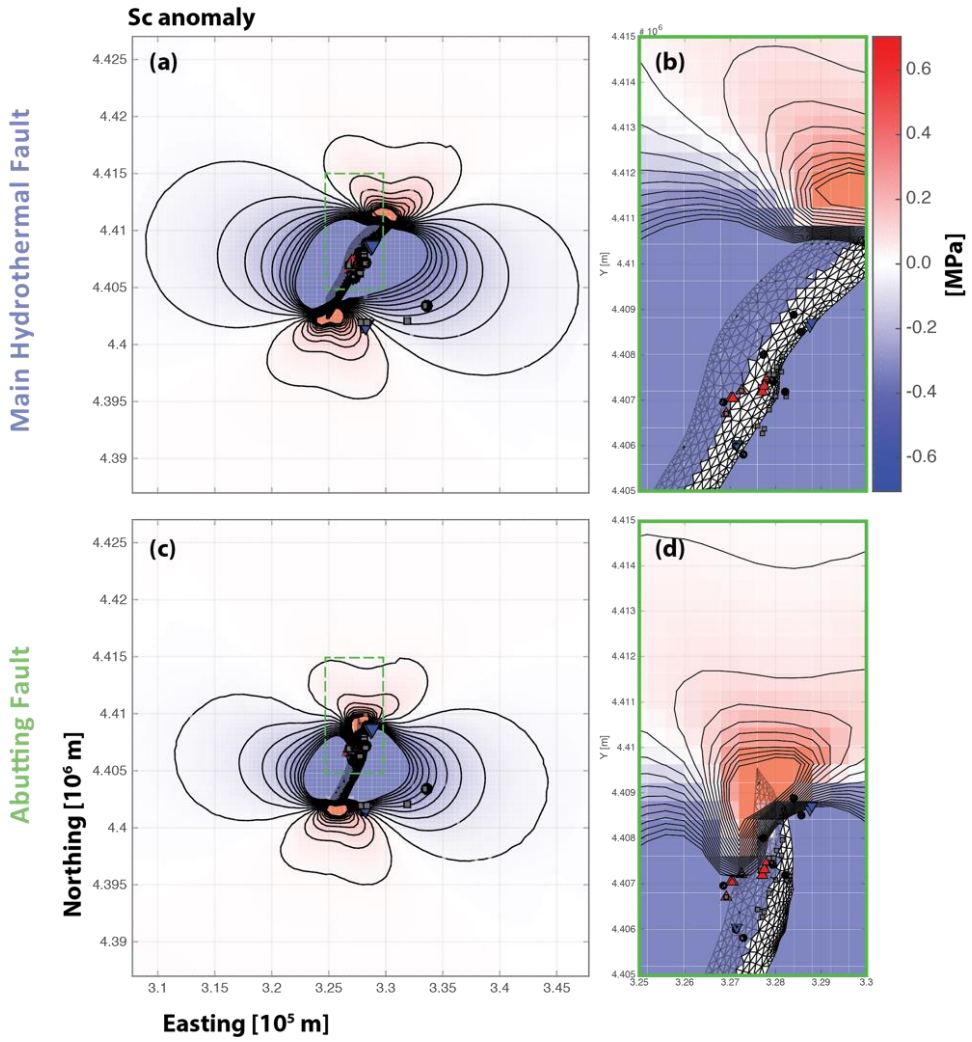

Figure 12: Local maximum coulomb stress computed from slip on individual segments: (a) $Sc^{(max)}$ due to slip on the main segment associated with production and hydrothermal activity (colored as in Figure 1, 2 and 11) and (b) an enlarged view showing the distribution of active production wells (red triangles), injectors (blue triangles), and idle wells (gray triangles). (c) $Sc^{(max)}$ due to slip on the fault segment abutting the main segment and (d) enlarged view showing the relative position of wells to $Sc^{(max)}$.

5. SUMMARY AND CONCLUSION

This preliminary study investigates the relationship between fault geometry and associated stress perturbations resulting from fault slip driven by remote stresses. These stress perturbations predict volumes more prone to fracture and dilation that could provide the connected porosity to support a hydrothermal system. From our investigation of the normal fault system at the Brady Geothermal field, we find that S_c^{max} is enhanced in areas of near fault tips and some geometries of overlapping fault segments. The greatest area of enhancement is achieved when fault segments underlap and have a left step and separation of the fault segments is from 0 to 1.5 the segment strike length. Conversely, S_c^{max} is reduced or where faults are poorly oriented to slip, for right-steps and for extensive overlap between fault segments. The models of idealized fault geometries also suggest that en echelon faults provide the most optimal conditions at relatively large separations, whereas horsts lead to even more favorable conditions at small separation. In general, underlapping horsts provide the most optimal conditions. We also learn that the current configuration of active normal fault segments at Brady does not fall within this range at the reservoir depth because of its much smaller overlap (~0.01x fault strike length) and separation (~0.03x fault strike length) at the higher coefficient of friction of 0.90 to 0.93. However: (1) measured coefficients of friction can be much smaller in some rock at Brady, allowing large areas to be critically stressed; (2) the current geometry of Brady likely evolved from more isolated faults with large underlap and separation corresponding to the more favorable conditions. These models do

not yet address the role of intersections and bends which are also characteristic of Brady; these are the subject of on-going analysis. Relative misalignment of faults, i.e., different strike, appear to play a potentially important role in promoting fracturing over large volumes.

Slip tendency analyses of the detailed faults show that portions of the faults in the vicinity of production wells, hydrothermal features, and active seismicity are critically stressed to slip. Additionally, dilation is favored in some of the areas where slip is promoted. Elastic models in which these faults individually slip reveals that the main hydrothermal fault largely lowers S_c^{max} within the vicinity of production wells i.e. near a fault bend with a left step geometry, whereas the abutting southern fault segment enhances S_c^{max} at its northern tip. We will next consider the role of a splay segment to the north and the extensive east dipping normal fault to the east which defines a horst structure. Results to date suggest that these faults, either individually or through mechanical interaction may play a critical role in promoting local fracturing. The nature of this interaction will be explored using the slip distributions established by these faults from the geologic model and the corresponding slip distributions in the elastic model.

ACKNOWLEDGEMENTS

This work was cofounded by Lawrence Berkeley National Laboratory with particular help from Dr. Lawrence Hutchings and the Department of Energy Geothermal Technologies Program FOA DE-FOA-0000522; award number DE –EE0005510. We would also like to acknowledge ORMAT for support and sharing critical data and insights concerning Brady. Egbert Jolie, Inga Moeck, and James Faulds have generously shared structural insights as well as their 3D geological modeling, enabling important elements of this analysis.

REFERENCES

Ali, S.T., Akerley, J., Baluyut, E., Davatzes, N.C., Feigl, K.L. Foxall, W., Mellors, R.J., Spielman, P., Wang, H.F., and Zemach, E.: Deformation at Brady Hot Springs (Nevada) Geothermal Field Measured by Time Series Analysis of InSAR Data, Manuscript, (2014), 21 p.

Ali, S.T., Davatzes, N.C., Feigl, K.L., Wang, H.F., Foxall, W., Mellors, R.J., Akerley, J., Zemach, E., and Spielman, P.: Deformation at Brady Hot Springs Geothermal Field Measured by Time Seires Analysis of InSAR Data, *Proceedings*, 40th Workshop on Geothermal Reservoir Engineering, Stanford University, Stanford, CA (2015).

Ali, S.T., Akerley, J., Baluyut, E.C., Cardiff, M., Davatzes, N.C., Feigl, K.L., Foxall, W., Fratta, D., Mellors, R.J., Spielman, P., Wang, H.F., and Zemach, E.: Time-Series Analysis of Surface Deformation at Brady Hot Springs Geothermal Field (Nevada) using Interferometric Synthetic Aperture Radar, *Geothermics*, **61**, (2016), 114-120.

Barton, C.A., Zoback, M.D., and Moos, D.: Fluid Flow along Potentially Active Faults in Crystalline Rock, *Geology*, **23 (8)**, (1995), 683-686.

Bell, J.W.: Quaternary Fault Map of Nevada, Reno Sheet, Nevada Bureau of Mines and Geology Map 79, (1984).

Benoit, W.R., Hiner, J.E., and Forest, R.T.: Discovery and Geology of the Desert Peak Geothermal System: A Case History, *Nevada Bureau of Mines and Geology Bulletin*, **97**, (1982).

Byerlee, J.D.: Friction of Rocks, *Pure and Applied Geophysics*, **116**, (1978), 615-626.

Caine, J.S., Evans, J.P., and Forster, C.B.: Fault Zone Architecture and Permeability Structure, *Geology*, **24**, (1996), 1025-1028.

Caskey, S.J., and Wesnouskey, S.G.: Active Faulting and Stress Redistribution in the Dixie Valley, Beowawe, and Bradys Geothermal Field: Implications for Geothermal Exploration in the Basin and Range: 25th Workshop on Geothermal Reservoir Engineering, Stanford University, Stanford, CA (2000).

Curewitz, D., and Karson, J.: Structural Settings of Hydrothermal Outflow: Fracture Permeability Maintained by Fault Propagation and Interaction, *Journal of Volcanology and Geothermal Research*, **79**, (1997), 149-168.

Coolbaugh, M.F., Sladek, C., Kratt, C, and Edmondo, G.: Digital Mapping of Structurally Controlled geothermal Features with GPS Units and Pocket Computers, *Geothermal Resources Council Transactions*, **28**, (2004), 321-326.

Crider, J.G., and Pollard, D.D.: Fault Linkage: Three-Dimensional Mechanical Interaction between Echelon Normal Faults, *Journal of Geophysical Research*, **103(B10)**, (1998), 24373-24391.

Crouch. S.L., and Starfield, A.M.: Boundary Element Method in Solid Mechanics: With Applications in Rock Mechanics and Geological Engineering: London, Unwin Hyman, (1983).

Davatzes, N.C., Feigl, K.L., Mellors, R.J., Foxall, W., Wang, H.F., and Drakos, P.: Preliminary investigation of Reservoir Dynamics Monitored Through Combined Surface Deformation and Micro-Earthquake Activity: Brady's Geothermal Field, Nevada, *Proceedings*, 38th Workshop on Geothermal Reservoir Engineering, Stanford University, Stanford, CA (2013).

Davatzes, N.C., Feigl, K., Wang, H., Mellors, R., Foxall, W., Drakos, P., Ali, T., and Singh, A.: Monitoring EGS Stimulation and Reservoir Dynamics with InSAR and MEQ, *Geothermal Technologies Office Peer Review*, DE-EE0005510 (2015) 4 p.

Faulds, J.E., and Garside, L.J.: Preliminary Geologic Map of the Desert Peak – Brady Geothermal Fields, Churchill County, Nevada, *Nevada Bureau of Mines and Geology*, Open-File Report 03-27 (2003).

Faulds, J.E., Coolbaugh, M.F., Benoit, D., Oppliger, G., Perkins, M., Moeck, I., and Drakos, P.: Structural Controls of Geothermal Activity in the Northern Hot Springs Mountains, Western Nevada: The Tale of three Geothermal Systems (Brady's, Desert Peak, and Desert Queen), *Geothermal Resources Council Transactions*, **24**, (2010), 675-683.

Faulds, J., Moeck, I., Drakos, P., and Zemach, E.: Structural Assessment and 3D Geological Modeling of the Brady's Geothermal Area, Churchill County (Nevada, USA): A Preliminary Report, *Proceedings*, 35th Workshop on Geothermal Reservoir Engineering, Stanford University, Stanford, CA (2010).

Faulds, J.E., and Hinz, N.H.: Favorable Tectonic and Structural Settings of Geothermal Settings in the Great Basin Region, Western USA: Proxies for Discovering Blind Geothermal Systems, *Proceedings*, World Geothermal Congress, Melbourne, Australia, CA (2015).

Gaucher, E., Schoenball, M., Heidbach, O., Zang, A., Fokker, P., van Wees, J., and Kohl, T.: Induced Seismicity in Geothermal Reservoirs: Physical Processes and Key Parameters, *Proceedings*, World Geothermal Congress, Melbourne, Australia, (2015).

GeothermEx: Evaluation of the Geothermal Resource at Brady's Hot Springs, Nevada, GeothermEx, Inc., Richmond, CA, 140 p, (1992).

Hanano, M.: Contribution of Fractures to Formation and Production of Geothermal Resources, *Renewable and Sustainable Energy Reviews*, **8**, (2004), 223-236.

Heffer, K.: Geomechanical Influences in Water Injection Projects: An Overview, *Oil and Gas Science and Technology – Rev. IFP*, **57(5)**, (2002), 415-422.

Jaeger, J.C., Cook, N.G.W., and Zimmerman, R.W.: *Fundamentals of Rock Mechanics*. 4th ed. Blackwell Publishing Ltd, Oxford, (2007).

Jolie, E., Faulds, J., and Moeck, I.: The Development of a 3D Structural –Geological Model as Part of the Geothermal Exploration Strategy – A Case Study from the Brady's Geothermal System, Nevada, USA, *Proceedings*, 37th Workshop on Geothermal Reservoir Engineering, Stanford University, Stanford, CA (2012).

Jolie, E.: Detection and Characterization of Permeable Fault Zones by Surface Methods in the Basin and Range Province, USA [*Dissertation*]: der Technischen Universität Berlin, 132 p (2014).

King, G.C.P., Stein, R.S., and Lin, J.: Static Stress Changes and the Triggering of Earthquakes, *Bulletin of the Seismological Society of America*, **84(3)**, (1994), 935-953.

Kratt, C., Coolbaugh, M., and Calvin, W.: Remote Detection of Quaternary Borate Deposits with ASTER Satellite Imagery as a Geothermal Exploration Tool, *Geothermal Resource Council*, 30, (2006), 435-440.

Lockner, D.A., and Beeler, N.M. (2002), Rock Failure and Earthquakes, in *International Handbook of Earthquake and Engineering Seismology*, Chapter 32, edited by W .. Lee, H. Kanamori, P. Jennings and C. Kisslinger, Academic Press, Amsterdam, (2002), 505-537.

Lutz, S.J., Hickman, S., Davatzes, N.C., Zemach, E., Drakos, P., and Robertson-Tait, A.: Rock Mechanical Testing and Petrologic Analysis in Support of Well Stimulation Activities at the Desert Peak Geothermal Field, Nevada, *Proceedings*, 35th Workshop on Geothermal Reservoir Engineering, Stanford University, Stanford, CA, (2010).

Lutz, S.J., Zutshi, A., Robertson-Tait, A., Drakos, P., and Ezra, Z.: Lithologies, Hydrothermal Alteration, and Rock Mechanical Properties in Wells 15-12 and BCH-3, Brady's Hot Springs Geothermal Field, Nevada, *Geothermal Resources Council Transactions*, **35**, (2011), 469-476.

Maerten, L., Gillespie, P., and Pollard, D.D.: Effects of Local Stress Perturbation on Secondary Fault Development, *Journal Structural Geology*, **24**, (2002), 145-153.

Micklethwaite, S., Sheldon, H.A., and Baker, T.: Active Fault and Shear Processes and their Implications for Mineral Deposit Formation and Discovery, *Journal of Structural Geology*, **32**, (2010), 151-165.

Moeck, I., and Backers, T.: Fault Reactivation Potential as Critical Factor during Reservoir Stimulation, *First Break*, **29**, (2011), 67-74.

Moos, D., Hickman, S, Blake, K., and Davatzes, N.C.: Stress Field Analysis; *In:* ORMAT (2011), Brady's EGS Project: Phase I: Studies and Engineering Summary Report, DE-FG36-08GO18200 (confidential), (2011, unpublished), 114 p.

Morris, A.P., Ferrill, D.A., and Henderson, D.B.: Slip Tendency and Fault Reactivation, *Geology*, **24**, (1996), 275-278.

Nathwani, J., Majer, E., Boyle, K., Rock, D., Peterson, J., and Jarpe, S. (2011), DOE Real-Time Seismic Monitoring at Enhanced Geothermal System Sites, *Proceedings*, 36th Workshop on Geothermal Reservoir Engineering, Stanford University, Stanford, CA (2011).

Shevenell, L., Oppliger, G., Coolbaugh, M. & Faulds, J.: Bradys (Nevada) InSAR Anomaly Evaluated With Historical Well Temperature and Pressure Data, *Geothermal Resources Council Transactions*, **36**, (2012), 1383-1390.

Siler, D.L. and Faulds, J.E.: Three-Dimensional Geothermal Fairway Mapping: Examples form the Western Great Basin, USA, *Geothermal Resource Council*, 37, (2013), 327-332;

Siler, D.L., Faulds, J.E., and Hinz, N.H.: Regional and Local Geothermal Potential Evaluation: Examples from the Great Basin, USA, Iceland and East Africa, *Proceedings*, World Geothermal Congress, Melbourne, Australia, (2015).

Swyer, M.W., and Davatzes, N.C.: Using Boundary Element Modeling of Fault Slip to Predict Patterns of Stress Perturbations and Related Fractures in Geothermal Reservoirs and Explore Parameter Uncertainty, *Proceedings*, 37th Workshop on Geothermal Reservoir Engineering, Stanford University, Stanford, CA (2012).

Swyer, M.W., and Davatzes, N.C.: Evaluating the Role of the Rhyolite Ridge Fault System in the Desert Peak Geothermal Field with Robust Sensitivity Testing through Boundary Element Modeling and Likelihood Analysis, *Proceedings*, 38th Workshop on Geothermal Reservoir Engineering, Stanford University, Stanford, CA (2013).

Tamagawa, T., and Pollard, D.D.: Fracture Permeability created by Perturbed Stress Fields around Active Faults in a Fractured Basement Reservoir, The *American Association of Petroleum Geologists Bulletin*, **92(6)**, (2008), 743-764.

TerraTek Report TR11-403124: Petrologic Evaluation of Selected Well Cuttings, Brady's Hot Springs Well 15-12, Churchill County, Nevada: *Report prepared for Ormat Nevada* (May 2011, 33 p.), Electronic Report.

TerraTek Report TR11-403371: Geomechanics and Petro-Physical Characterization of Selected Materials: BCH-3 Well (July 2011, 70 p.); Petrologic Evaluation of Selected Core Samples - Bradys Hot Springs Well BCH-03 - Churchill County, Nevada (May 2011, 20 p.): *Reports prepared for Ormat Nevada*, electronic report.

Thomas, A.L.: Poly3D: A Three-Dimensional, Polygonal-Element, Displacement Discontinuity Boundary Element Computer Program with Applications to Fractures, Faults, and Cavities in the Earth's Crust: M.Sc. Thesis, Stanford University, Stanford, CA, 62 p (1993).

Zoback, M.D.: *Reservoir Geomechanics*, Cambridge University Press, Cambridge, U.K., (2007).